Activating Mn_3O_4 by Morphology Tailoring for Oxygen Reduction Reaction

Jing Liu[a,1], Luhua Jiang[a,*], Tianran Zhang[a], Jutao Jin[a], Lizhi Yuan[a,b], Gongquan Sun[a,*]

[a] Dalian National Laboratory for Clean Energy, Dalian Institute of Chemical Physics, Chinese Academy of Sciences, Dalian, 116023, China
[b] Graduate University of Chinese Academy of Sciences, Beijing, 100039, China

ABSTRACT

Oxygen reduction reaction (ORR) is becoming increasingly important with the development of fuel cells and metal-air batteries. Manganese oxides have been one of the focuses of recent research for Pt-alternative ORR catalysts. However, the structure-activity relationships of manganese oxides have not been well studied or understood. In the present work, we report a new finding that there is a strong dependence of the ORR activity of Mn_3O_4 on its morphology. By adopting different solvents in the wet-chemical synthesis, we are able to tailor the morphology of Mn_3O_4 from nanoparticles (NP-L, 12.5 nm and NP-S, 5.95 nm) to nanorods (NR, exposure of Mn_3O_4 (101)) and nanoflake (NF, exposure of Mn_3O_4 (001)). Surprisingly, surface-specific activity of NF toward the ORR was found to be one order of magnitude higher than NP-L. The morphology-activity relationships of Mn_3O_4 were further studied through a combination of electrochemical experiments and density functional theory (DFT) calculations. It was discovered that the formation of *OOH, concomitant with the first electron transfer, is the potential determining step, which is thermo-dynamically more facile on Mn_3O_4 (001) than (101) plane. The underlying mechanism could be ascribed to the strong interaction between O_2 and Mn_3O_4 (001) surface as indicated by the DFT calculations. The study enlarges our understanding of Mn_3O_4 catalysis and provides clues for rational design of highly efficient transitional metal oxide electrocatalysts for the ORR.

© 2016 Published by Elsevier Ltd.

1. Introduction

Oxygen reduction reaction (ORR), as the main cathodic reaction of fuel cells and metal-air batteries, is of great technical and fundamental importance [1]. The sluggish kinetics of the ORR requires a highly active catalyst to activate oxygen molecules. For decades, Pt based materials are known to be the most active electrocatalyst for the ORR, but the high price and scarce reserve of Pt limit its application in large scale [2,3]. Thus, to explore Pt-alternative catalysts [4,5] became an urgent task. In the past decades, tremendous efforts have been devoted to metal oxides, e.g. perovskites, spinels and so on [6–9]. Among them, manganese oxides are a class of attractive candidate due to their promising activity for the ORR together with the low cost and abundant reserves in the earth [10–12]. By tuning the electronic state of Mn [13], the oxygen vacancies in surface of manganese oxides [14], as

well as promoting the interaction between manganese oxides and carbon supports [15], the ORR activity of manganese oxides has been improved.

In addition to the above mentioned approaches, crystal facet engineering has demonstrated to be an effective way to modify the catalytic activity [16,17], since the reactivity and selectivity of catalysts depend greatly upon the arrangement manner of surface atoms and the number of dangling bonds on different crystal planes for structure-sensitive reactions, such as CO oxidation reaction and ORR [18]. Previously, rod-shaped Co_3O_4 with a higher exposure of the reactive (110) planes, which are rich in catalytically active Co^{3+} species, was reported to display particularly high activity towards low-temperature CO oxidation [19]. Recently, Xiao et al. reported that the catalytic activity of ORR depends on the crystal planes of the Co_3O_4 and follows the order {111} > {100} > {110} [20]. It has been also reported that differently shaped MnO_x nanocrystals, such as cubes, octahedral, wires etc., performed differently in supercapacitor and oxidation of methylene blue [21,22]. However, little is known about the relationship between crystal planes of manganese oxides and their ORR activity. Considering ORR is a surface sensitive reaction, an in-depth understanding of how the crystal plane affects the ORR activity of

---

* Corresponding authors. Tel.: +86 411 84379063; fax: +86 411 84379063.
  E-mail addresses: sunshine@dicp.ac.cn (L. Jiang), gqsun@dicp.ac.cn (G. Sun).
1 Present address: Department of Chemical and Biomolecular Engineering, University of California, Los Angeles, CA, 90095, USA.

manganese oxides is therefore highly desirable for guiding the development of advanced ORR electrocatalysts.

Manganese oxides are complex in morphology and metal valence, which makes identifying the surface structure-activity relationship a challenging task. In this work, considering the hausmannite Mn_3O_4 is the most stable type among the manganese oxides under the electrochemical testing condition [13], it was selected to investigate the morphology dependence of the ORR activity. To minimize the influence of surface oxygen vacancies and the defects on the ORR activity, the Mn_3O_4 crystals are intentionally synthesized in dozens of nanometer or micrometer scale with different morphologies. The ORR catalytic activity is correlated with the planes of the Mn_3O_4 nanocrystal experimentally and theoretically.

2. Experimental

2.1. Preparation of Mn_3O_4 nanocrystals

The synthesis of Mn_3O_4 of different morphologies is described as follows. For the Mn_3O_4 nanoparticles of large particle size (denoted as NP-L), 0.5 g manganese acetate was dissolved in 25 mL ethanol followed by adding 2.5 mL 25 w.t. % $NH_3 \cdot H_2O$ to the above solution. The mixture was refluxed at 100 °C till the mixture became brown. The mixed suspend was centrifuged to obtain a brown precipitate, after washed and dried overnight in a vacuum oven. Interestingly, Mn_3O_4 nanoparticles with smaller size could be obtained, when N, N-dimethylformamide (DMF) was exploited as the solvent to replace ethanol. The particle size of the Mn_3O_4 nanocrystals became smaller, which is denoted as NP-S. As for the synthesis of Mn_3O_4 nanoflakes (denoted as NF), the protocol was the same as above except using water as the solvent.

The Mn_3O_4 nanorods (denoted as NR) were synthesized adopting a previously reported method [13]. Specifically, 0.3 g of $KMnO_4$ dissolved in 30 mL of deionized (DI) water was added into a 100 mL stainless steel autoclave, and then 0.3 mL of ethanol was added dropwise under stirring. After that, the autoclave was sealed and kept at 130 °C in oil bath for 24 h with magnetic stirring. After cooling down to room temperature naturally, the product was filtered and washed by copious DI water and dried in a vacuum oven at 80 °C. The obtained MnO_x was denoted as MnO_x-AP. The MnO_x-AP was subsequently calcined at 600 °C in tube oven protected by nitrogen gas for 6 h to obtain Mn_3O_4 nanorods.

2.2. Physical Characterization

X-ray diffraction (XRD) measurements were performed on a Rigaku X-2000 diffractometer using Cu Kα radiation with a Ni filter. The tube voltage and the tube current were maintained at 40 kV and 100 mA, respectively. The sample was scanned from 15° to 85° (2θ) at a scan rate of 5° min^{-1}. Transmission electron microscopy (TEM) images of the catalysts were taken on FEI Tecnai G2 F30 system. The microscope was operated at an accelerating voltage of 200 kV. Atomic force microscopy (AFM) images of nanorod and nanoflake were taken in tapping mode using an AFM (Veeco, Dimension® EdgeTM). Scanning electron microscopy (SEM) experiments were conducted on a JEOL JSM-6700 FE-SEM. Nitrogen sorption isotherms were measured at 77 K with a Micromeritics ASAP 2020 analyzer. The samples were degassed in vacuum at 120 °C for 10 hours. The specific surface areas (SA) were calculated by the Brunauer-Emmett-Teller (BET) in a relative pressure ranging from 0.04 to 0.25. X-ray photoelectron spectroscope (XPS, ESCALAB 250Xi) with X-ray sources of Al Kα was used to investigate the surface valence of the Mn in catalysts. All spectra were calibrated to 284.6 eV, the line position of adventitious carbon.

2.3. Electrochemical Measurements

For the electrochemical measurements, the catalyst ink was prepared as following: Three milligram of Mn_3O_4 powder plus 2 mg of carbon powder (Vulcan XC-72, Cabot Corp., pre-treated in 5 M HNO_3 at 120 °C for 6 hrs, denoted as XC-O) to increase the conductivity were mixed with 2 mL of ethanol and 30 μL of Nafion (5 wt % Dupont, USA). After ultrasonically blending for 15 min, 20 μL of the ink was pipetted on the glassy carbon disk. The electrode was dried under a smooth flow of N_2. The electrochemical setup is comprised of a computer controlled potentiostat, a radiometer speed control unit from Pine Instrument Company (MSRX Speed control), and a rotating disk electrode radiometer. The rotating disk electrode (RDE) is 5.0 mm in diameter. The electrochemical experiments were carried out with a conventional three-electrode cell. A Pt wire counter electrode and a Hg/HgO reference electrode in a 1 M NaOH solution were used. The catalytic activity of the Mn_3O_4 catalysts towards the ORR was tested in O_2 saturated 1 M NaOH solution by linear sweep voltammetry at a scan rate of 1 mV s^{-1}. All potentials initially measured versus the Hg/HgO electrode were converted to values vs. reversible hydrogen electrode (RHE) after calibration.

2.4. DFT calculation

All the corresponding calculations were performed by the Vienna ab initio simulation package (VASP) using periodic density functional theory (DFT) [23]. Projector augmented wave (PAW) method with generalized gradient approximation (GGA) of Perdew–Wang 1991 (PW91) was employed to describe valence-electron interactions [24]. The integration of the Brillouin zone was conducted using a $3 \times 3 \times 1$ Monkhorst–Pack grid. Energy cutoff was set at 400 eV and electron smearing was employed using Gaussian smearing technique with a width of 0.2 eV. Spin polarization calculation was carried out for all possible structures with the bottom two layers of the surface being fixed. Electronic energies were computed with the SCF tolerance of 10^{-5} eV and total forces were converged to less than 0.02 eV/Å.
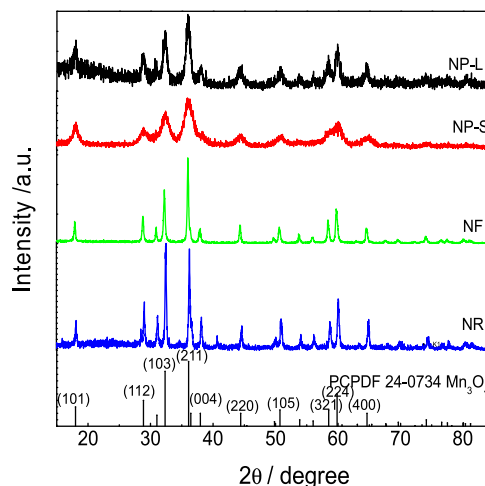

Fig. 1. XRD patterns of Mn_3O_4 nanocystals. The diffraction peak position and the relative intensity of the standard of Mn_3O_4 sample (PCPDF 24-0734) is displayed at the bottom of the figure.

3. Results and discussion

3.1. Physical characterization of the Mn₃O₄ catalysts

The crystal structure of the four Mn₃O₄ samples were investigated by XRD. As shown in Fig. 1, all samples give out diffraction peaks at 32.3, 36.1 and 59.8°, which can be indexed to (103), (211) and (224) crystal facets of tetragonal Mn₃O₄ (PCPDF 24-0734). No extra peaks are observed, confirming the high purity of the samples in phases [25]. It is observed that the diffraction peak became stronger and sharper with the sequence of NP-S, NP-L, NF and NR, indicating the formation of well-defined crystalline and the increase of the particle size, which is consistent with the statistic result from TEM as well as BET surface area that obtained from N₂ adsorption measurements.

To discriminate the morphology and the exposed crystal planes, TEM images of NP-L, NF and NR are displayed in Fig. 2a-c. For NP-L in Fig. 2a, synthesized with ethanol as the solvent, it contains nanoparticles approximate to spherical in shape with an average size of 12.5 nm (Fig. 2a & Fig. S1). By adopting alternative solvent DMF, the average size of the spherical particles could be reduced to 5.95 nm (NP-S, Fig. S2). As shown in Fig. 2b, the particles in NF are quasi-square with edge-length of about 40 nm. The thickness of each square is around 18 nm observed from the AFM image (Fig. S3). For the NR, it is composed of nanorods with the average dimension of around 40 nm in diameter and 1.6 μm in length (Fig. 2c and Fig. S4). The morphologies of the samples are further confirmed by the SEM images (Fig. S5). In the HRTEM images of the representative NP-L, NF and NR particles, as shown in Fig. 2d-f, the distinguishable lattice fringe spacing is 0.29, 0.47 and 0.49 nm, which is well consistent with the lattice distance of Mn₃O₄ (200), (002) and (101) planes[26], [22], respectively. Since the lattice plane (002) is parallel to the face of the NF, {001} planes are referred to be the dominant exposed planes of the NF [26,27]. The growth plane of the NR have {101} planes in the longitudinal growth direction, {101} planes are shown to be the preferentially

exposed planes of the NR [28]. The inserts of Fig. 2d-f display the corresponding Fast Fourier Transform (FFT) patterns of the selected particles, which also confirms the exposed crystal planes being the ones observed in the HRTEM images.

The surface elemental composition of the samples was characterized by XPS. The high resolution Mn 2p XPS spectra for all the samples are of similar characteristics (Fig. 3a). The binding energy (BE) of Mn $2p_{3/2}$ is 641.9 eV, and the spin orbit splitting between Mn $2p_{3/2}$ and Mn $2p_{1/2}$ is 11.6 eV, which matches well with the values reported for hausmannite Mn₃O₄ [29]. The oxidation state of Mn is further analyzed by deconvoluting Mn 2p3/2 peak into three components with binding energies of 640.8, 641.9 and 644.5 eV which corresponds to Mn^{2+}, Mn^{3+}, and the shakeup peak, respectively. By integrating the areas of the peak for Mn^{2+} and Mn^{3+}, the surface ratio of Mn^{3+} to Mn^{2+} for NP-L, NP-S, NF and NR is calculated to be 0.72, 0.89, 2.37 and 0.97, respectively. This indicates that NF possesses the highest surface Mn^{3+} concentration, followed by NR, NP-S and NP-L, which can be attributed to the different arrangement manner of surface atoms on different crystal planes. The O1s spectra for the samples as shown in Fig. 3b, exhibits a main peak located at 529.6 eV and a shoulder peak located at 531.3 eV, which are assigned to the lattice oxygen bonding with Mn(O_{latt}) and the oxygen species adsorbed on the surface(O_{ads}), respectively [13,30]. The relative intensity of O_{latt}/O_{ads} follows the trend of NP-S (1.45) < NF (2.41) < NP-L (2.82) < NR (3.17). Such an order is related with two factors, (i) the crystallinity of samples (the higher the crystallinity, the higher the ratio of the O_{latt}/O_{ads}) and (ii) the surface energy. The higher O_{latt} percentage for the NR, NP-L and NF is agreeable with their high crystallinity, while the relatively low O_{latt} percentage for the NP-S is due to its poor crystallinity. Among NR, NP-L and NF, the highest O_{ads} percentage for the NF is related with the exposed Mn₃O₄ (001) surface, which is of higher energy compared to the NP-L and NR with the exposed Mn₃O₄ (101) surface. The nitrogen adsorption-desorption isotherms of NF and NR, as shown in Fig. 4, display a typical type III
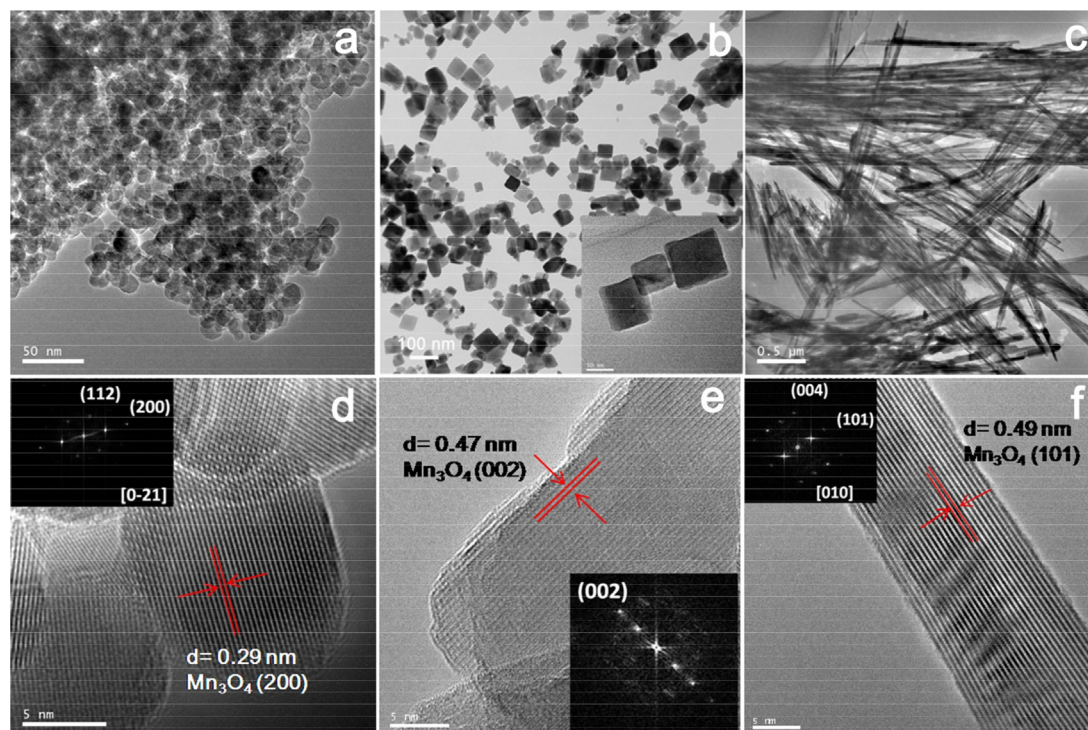

Fig. 2. The typical TEM bright-field images of Mn₃O₄ nanocystal with different morphologies (a) nanoparticles (NP-L), (b) nanoflakes (NF) and (c) nanorods (NR), and the corresponding HRTEM images of a single Mn₃O₄ nanocrystal (d) NP-L, (e) NF and (f) NR (inserts are the corresponding FFT patterns).
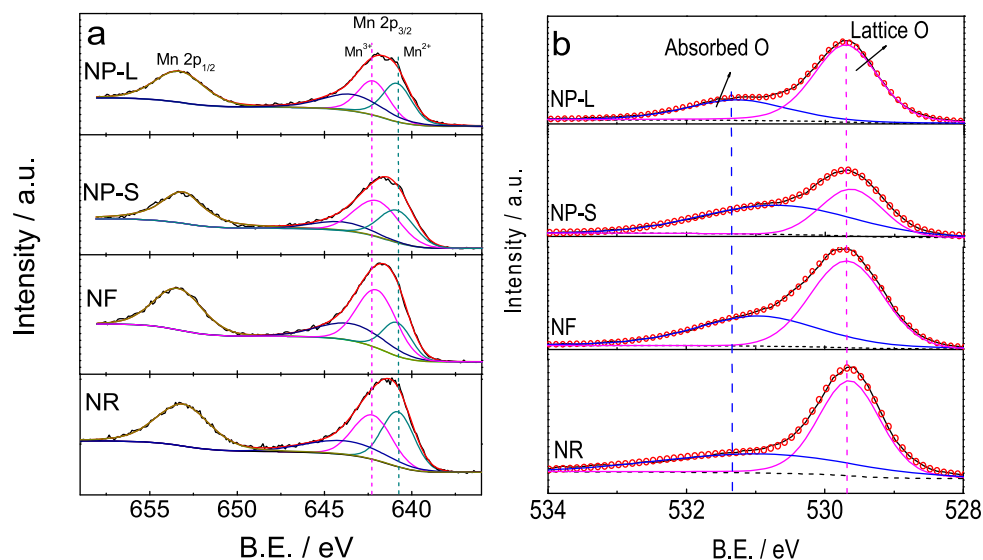
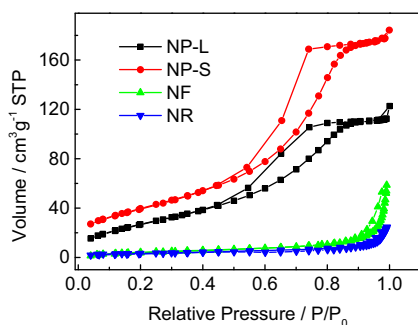**Fig. 3.** High revolution Mn2p (a) and O1s (b) XPS spectra of Mn_3O_4 samples.

Fig. 4. N_2 adsorption-desorption isotherms of Mn_3O_4 samples.

adsorption-desorption isotherms, indicating that the sample contains macropores (> 50 nm). The macropores should be interparticle pores formed by the Mn_3O_4 nanoflakes or nanorods cumulation. The absence of micro-/mesopores in NF and NR suggest perfect Mn_3O_4 crystals. Such a perfect surface at nano- or microscale but with preferential crystallographic orientation nicely provide a chance to investigate the catalytic activity dependence on the Mn_3O_4 crystal planes. In contrast, the adsorption-desorption isotherms of the NP-L and NP-S are typical V-type ones, suggesting mediate sized pores ($2 \sim 50$ nm) in samples. Since NP-L and NP-S contain Mn_3O_4 spherical nanoparticles with the average size of 12.5 and 5.95 nm, respectively, the surface may contain defects, especially for the NP-S composed of smaller particles. The BET surface areas for the four samples are listed in Table 1, i.e. NP-S (146.4 m^2/g), NP-L (106.2 m^2/g), NF (17.6 m^2/g) and NR (11.6 m^2/g). The larger surface area of the NP-L and NP-S are definitely ascribed to their smaller particle size than those of NF and NR.

3.2. Electrocatalytic properties of the Mn_3O_4 catalysts

The electrochemical surface features of the Mn_3O_4 samples are characterized by cyclic voltammery in a N_2-saturated 1 M NaOH solution with a scan rate of 10 mV s^{-1}, as shown in Fig. 5a. The voltammetric peaks are associated to a series of redox processes, including conversions of Mn (II) to Mn (III) in the range of 0.85–1.0 V and Mn (III) to Mn (IV) in the range of 1.0-1.2 V, suggested by in situ XANES [11]. For the nanoparticle samples (NP-L and NP-S), the anodic oxidation current starts at more negative potential than the NF and NR, and an anodic oxidation peak located at 1.0 V is observed for the NP-L and NP-S, which can be assigned to the oxidation of Mn (II) to Mn(III) [31]; but such a characteristic vanishes for NF and NR, indicating the surfaces might rich in Mn (III) cation instead of Mn (II). To make the comparison more clearly, the currents are normalized to the BET surface area. As shown in the normalized CV curves (Fig. 5b), the oxidation current for the Mn(III)/Mn(IV) couple is decreased in the sequence of NF, NR, NP-S and NP-L, indicating the surface concentration of Mn(III) cation. The result is in good agreement with the ratio of Mn(III)/Mn(II) analyzed by XPS analysis. By recording the CVs at different scanning rates (Fig. S6) and as a function of scanning rates, the double layer capacitance of the Mn_3O_4 is obtained and accordingly, the electrochemical surface active areas (ESCA) of the samples are estimated by assuming the specific capacitance of 0.04 mF cm^{-2} [32]. The calculated ECSA values are listed in Table 1, which follows the order of NP-S > NP-L > NF ≈ NR, a similar tendency as the BET surface area.

The catalytic activity of the Mn_3O_4 catalysts towards the ORR were tested in O_2-saturated 1 M NaOH solution and the ORR polarization curves are displayed in Fig. 6a. The limiting currents for all Mn_3O_4 catalysts are all around 0.45 mA. The electron transfer number (n) of the ORR (@ 0.5 V) over the Mn_3O_4 catalysts is calculated based on the ORR polarization curves recorded at

Table 1
Specific surface area (SA) and ORR currents (kinetic current, mass specific current and surface specific current) of Mn_3O_4 electrocatalysts taken at 0.83 V.

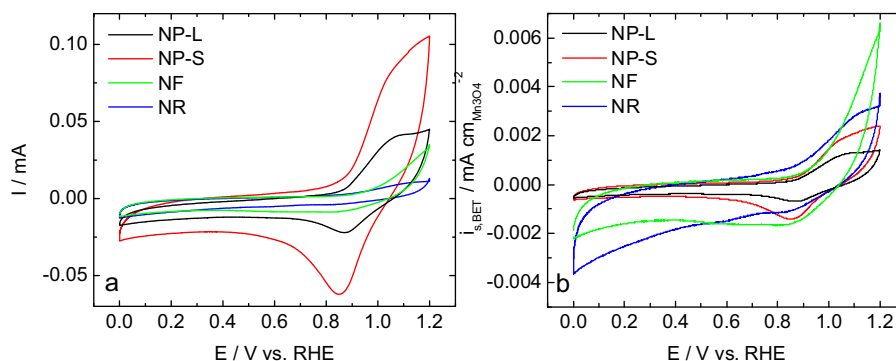|	SA_{BET}/m^2g^{-1}	ECSA/m^2g^{-1}	I_k/mA	i_m/mA mg$^{-1}Mn_3O_4$	$i_{s,BET}$/mA cm$^{-2}Mn_3O_4$	$i_{s,ECSA}$/mA cm$^{-2}Mn_3O_4$
NP-L	106.2	7.50	0.16	5.27	$5.02*10^{-3}$	$7.11*10^{-2}$
NP-S	146.4	23.33	0.49	16.40	$1.12*10^{-2}$	$7.00*10^{-2}$
NF	17.6	1.67	0.31	10.63	$5.87*10^{-2}$	0.62
NR	11.6	1.67	0.05	1.37	$1.44*10^{-2}$	0.10

Fig. 5. Cyclic voltammograms with the Mn_3O_4 as the working electrode before (a) and after (b) normalization in N_2 saturated 1 M NaOH. Scan rate: 10 mV s^{-1}.

different rotating speeds (Fig. S7) by the Levich equation. Over the NP-S, NP-L, NF and NR, the electron transfer number are 3.6, 3.1, 3.1 and 3.1, respectively. The half-wave potential ($E_{1/2}$) of the ORR for different Mn_3O_4 catalysts is in order of NP-S (0.83 V) > NF (0.82 V) > NP-L (0.80 V) > NR (0.78 V). The kinetic ORR currents (I_k) calculated via the Koutecky-Levich equation (Eq. (1)) are plotted in Tafel plots as shown in Fig. 6b.

$$\frac{1}{I} = \frac{1}{I_{lim}} + \frac{1}{I_k} \qquad (1)$$

The I_k of the samples in the mixed diffusion and kinetics controlled region also decrease in the order of NP-S > NF > NP-L > NR, which follows the trend of the $E_{1/2}$. Since the same amount of catalysts were used for tests, this trend stands for the order of mass specific activity. However, surface specific activity provides more information on the intrinsic catalytic ability of materials. To quantify the surface and mass specific activities of the Mn_3O_4 samples, both the

surface specific currents (i_s) and the mass specific currents (i_m) by normalizing I_k at 0.83 V (Fig. 6b) to the BET surface area as well as the ECSA and the mass of Mn_3O_4, respectively, are listed in Table 1 and visually displayed in Fig. 6c. The mass specific activity of NP-S is 16.40 mA mg^{-1}, which is the highest among the four samples and about 3 times of NP-L and 12 times of NR. The high mass activity of NP-S is ascribed mainly to the significantly higher surface area of the small Mn_3O_4 nanoparticles (146.4 m^2 g^{-1}) than larger particles (NP-L, 106.2 m^2 g^{-1}) and let alone the much larger nanoflakes (NF, 17.6 m^2 g^{-1}) and nanorods (NR, 11.6 m^2 g^{-1}), as listed in Table 1. For the NF, although the surface area is the lowest, the ORR mass activity is as high as 10.63 mA mg^{-1}, which is only lower than the NP-S (of the highest surface area). For NP-L and NP-S, the BET surface area of NP-S is about 1.4 times of NP-L (106.2 m^2 g^{-1}) and the ECSA of the former is about 3 times of the latter, correspondingly, the ORR current over the NP-S is about 3 times of that over the NP-L. This result suggests that the ECSA is highly
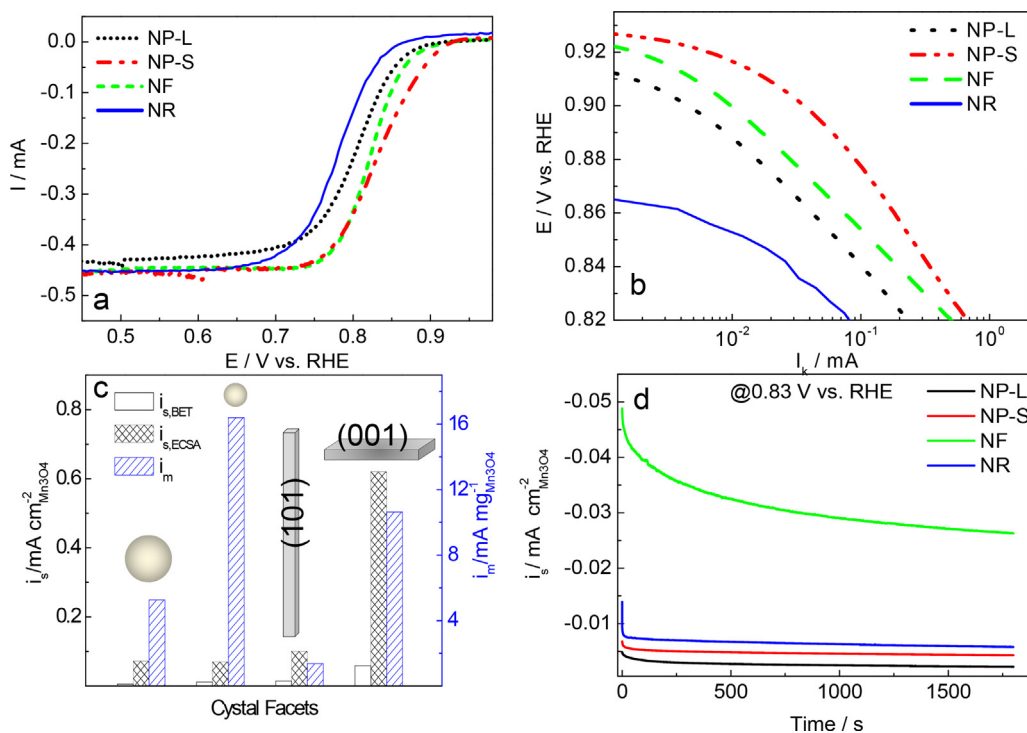

Fig. 6. ORR polarization curves (a) and the Tafel plots (b) of Mn_3O_4 nanocrystals with different morphologies in O_2 saturated 1 M NaOH. Scan rate: 1 mV s^{-1}; rotating rate: 1600 rpm. The histogram illustrates the crystal plane-dependent electrocatalytic activity of Mn_3O_4 nanocrystals for ORR. The mass specific (i_m) and surface specific (i_s) ORR currents were calculated from the kinetic currents (I_k) taken at 0.83 V in Fig. 6b (c). Chronoamperometric curves of the ORR recorded at 0.83 V with the Mn_3O_4 electrocatalysts in an O_2-saturated 1.0 M NaOH electrolyte (d).
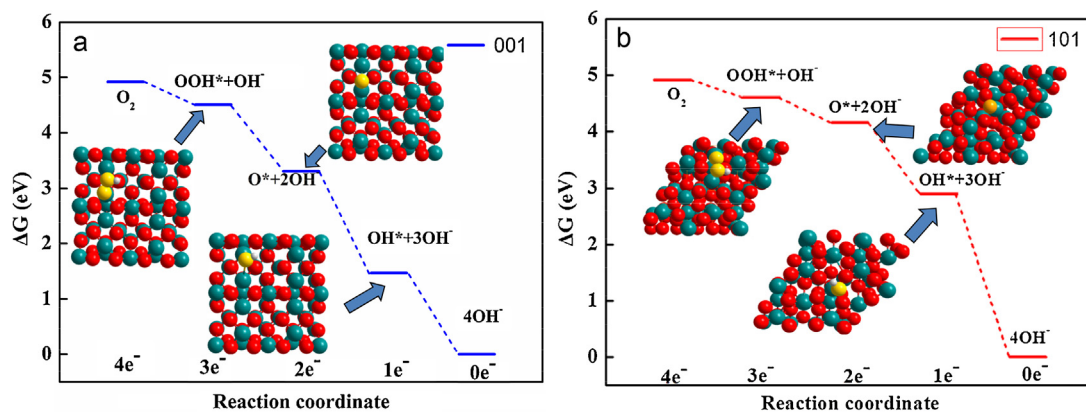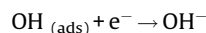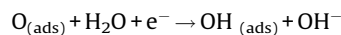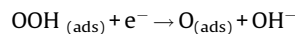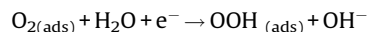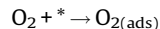
Fig. 7. The free energies for elementary steps along the reaction coordinate in ORR on the Mn_3O_4 (001) and (101) surface at U = 0.

related with the ORR activity, at least for the particles of the same morphology. For particles of different morphologies, e.g., NF, NR and NP-S, although the BET surface area of the NF is only 1/8 of the NP-S and the ECSA of the NF is just 1/14 of the NP-S, the i_k of the ORR is similar and thus, the specific current over the NF is almost 9 times of that over the NP-S, as listed in Table 1. NF and NR are of similar ECSA, however, the $i_{s,ECSA}$ for the NR is only 1/6 of that for the NF. Since both the NF and the NR monolith is in micrometer, which is less of oxygen vacancy and defects, the exciting promotion of the ORR activity for the NF is deduced coming from a remarkable shape effect, or precisely speaking, the preferentially exposed (001) facets.

The short-term stability of the samples were measured by chronoamerometry at 0.83 V for 1800s and the currents are presented in Fig. 6d. As it can be seen, the quasi-stable ORR currents at the end of 1800s follow the same order as the potential dynamic currents in Fig. 6c.

3.3. DFT calculation

To understand the intrinsic ORR activity of the specific surface planes of Mn_3O_4 nanocrystals, DFT calculation was performed on the Mn_3O_4 (001) and (101) surfaces. On these surfaces, the associative mechanism is presumed the predominant reaction pathway [31], which can be described as follows:

$$O_2 + * \rightarrow O_{2(ads)}$$

$$O_{2(ads)} + H_2O + e^- \rightarrow OOH_{(ads)} + OH^-$$

$$OOH_{(ads)} + e^- \rightarrow O_{(ads)} + OH^-$$

$$O_{(ads)} + H_2O + e^- \rightarrow OH_{(ads)} + OH^-$$

$$OH_{(ads)} + e^- \rightarrow OH^-$$

where * denotes a free site on the surface. Fig. 7 displays the calculated free energy profiles of oxygen activation over the Mn_3O_4 (001) and (101) surfaces. As we can see, at U = 0 eV, all the steps are downward on both surfaces, indicating the oxygen reduction reactions are thermodynamically favorite. The minimum energy change in the free energy profile is from the adsorbed O_2 to the adsorbed OOH, concomitant with the first electron transfer from Mn to oxygen molecule, likely to be potential determined step on both surfaces. The formation free energies of *OOH is 0.41 eV and

0.31 eV on Mn_3O_4 (001) and (101) surface, respectively, which implies the process on the surface of Mn_3O_4 (001) is more thermodynamically favorable than Mn_3O_4 (101). The facilitated O_2 adsorption on (001) surface than (101) may be related with the atomic arrangement on the top surface. (Fig. S8). Theoretically, (001) surface has Mn unsaturated coordinated with five oxygen, while the Mn in the (101) surface is saturated coordinated with four oxygen. Thus, the Mn valence on (001) surface is higher than that on (101) surface due to more dangling bonds presented on the former, which is in good agreement with the Mn valence analysis characterized by the CV and XPS. As discovered in the previous work [13,33], the ORR activity is related with the Mn with higher valence on the surface, i.e., Mn(III)/Mn(IV) species. [13,33]. Therefore, the NF and NR containing more Mn(III) on surface possess better catalytic activity than NP of lower surface Mn valence.

4. Conclusions

In summary, we have synthesized Mn_3O_4 nanocrystals with different preferential crystal planes by controlling the morphology. On this basis, the electrocatalytic activity of Mn_3O_4 for the ORR is correlated with the crystal planes. The results demonstrate that Mn_3O_4 nanoflakes with preferentially exposed (001) planes display significantly higher ORR activity than the Mn_3O_4 nanorods with preferentially exposed (101) planes; especially, it displays one order of magnitude higher ORR activity than Mn_3O_4 nanoparticles without preferentially exposed planes. Further DFT calculation suggests the first electron transfer process is the potential determining step of the ORR, which is thermodynamically more facile on (001) surface than on (101) surface. The discovered crystal plane depending ORR activity is expected to provide guidance for developing advanced metal oxide electrocatalysts for ORR.

Appendix A. Supplementary data

Supplementary data associated with this article can be found, in the online version, at http://dx.doi.org/10.1016/j.electacta.2016. 04.103.

References

[1] I. Katsounaros, S. Cherevko, A.R. Zeradjanin, K.J.J. Mayrhofer, Oxygen Electrochemistry as a Cornerstone for Sustainable Energy Conversion, Angew. Chem. Int. Edit. 53 (2014) 102–121.

[2] S.J. Guo, S. Zhang, S.H. Sun, Tuning Nanoparticle Catalysis for the Oxygen Reduction Reaction, Angew. Chem.Int. Edit. 52 (2013) 8526–8544.

[3] A. Morozan, B. Jousselme, S. Palacin, Low-platinum and platinum-free catalysts for the oxygen reduction reaction at fuel cell cathodes, Energy & Environ. Sci. 4 (2011) 1238–1254.

[4] Z. Chen, D. Higgins, A. Yu, L. Zhang, J. Zhang, A review on non-precious metal electrocatalysts for PEM fuel cells, Energy & Environ. Sci. 4 (2011) 3167–3192.

[5] F. Jaouen, E. Proietti, M. Lefevre, R. Chenitz, J.-P. Dodelet, G. Wu, H.T. Chung, C. M. Johnston, P. Zelenay, Recent advances in non-precious metal catalysis for oxygen-reduction reaction in polymer electrolyte fuel cells, Energy & Environ. Sci. 4 (2011) 114–130.

[6] J. Sunarso, A.A.J. Torriero, W. Zhou, P.C. Howlett, M. Forsyth, Oxygen Reduction Reaction Activity of La-Based Perovskite Oxides in Alkaline Medium: A Thin-Film Rotating Ring-Disk Electrode Study, J. Phy. Chem. C 116 (2012) 5827–5834.

[7] Y. Liang, H. Wang, J. Zhou, Y. Li, J. Wang, T. Regier, H. Dai, Covalent Hybrid of Spinel Manganese–Cobalt Oxide and Graphene as Advanced Oxygen Reduction Electrocatalysts, J. Am. Chem. Soc. 134 (2012) 3517–3523.

[8] J. Jin, F. Pan, L. Jiang, X. Fu, A. Liang, Z. Wei, J. Zhang, G. Sun, Catalyst-Free Synthesis of Crumpled Born and Nitrogen Co-Doped Graphite Layers with Tunable Bond Structure for Oxygen Reduction Reaction, ACS Nano 8 (2014) 3313–3321.

[9] H. Zhu, S. Zhang, Y.-X. Huang, L. Wu, S. Sun, Monodisperse $M_xFe_3-xO_4$ (M = Fe, Cu Co, Mn) Nanoparticles and Their Electrocatalysis for Oxygen Reduction Reaction, Nano lett. 13 (2013) 2947–2951.

[10] I. Roche, E. Chaînet, M. Chatenet, J. Vondrák, Durability of carbon-supported manganese oxide nanoparticles for the oxygen reduction reaction (ORR) in alkaline medium, J. Appl. Electrochem. 38 (2008) 1195–1201.

[11] F.H. Lima, M.L. Calegaro, E.A. Ticianelli, Investigations of the catalytic properties of manganese oxides for the oxygen reduction reaction in alkaline media, J. Electroanal. Chem. 590 (2006) 152–160.

[12] J. Vondrak, B. Klapste, J. Velicka, M. Sedlarikova, J. Reiter, I. Roche, E. Chainet, J.F. Fauvarque, M. Chatenet, Electrochemical activity of manganese oxide/carbon-based electrocatalysts, J. New Mater. Electrochem. Sys. 8 (2005) 209–212.

[13] Q. Tang, L. Jiang, J. Liu, S. Wang, G. Sun, Effect of Surface Manganese Valence of Manganese Oxides on the Activity of the Oxygen Reduction Reaction in Alkaline Media, ACS Catal. 4 (2013) 457–463.

[14] F. Cheng, T. Zhang, Y. Zhang, J. Du, X. Han, J. Chen, Enhancing Electrocatalytic Oxygen Reduction on MnO2 with Vacancies, Angew. Chem. Int. Edit. 125 (2013) 2534–2537.

[15] J. Duan, Y. Zheng, S. Chen, Y. Tang, M. Jaroniec, S. Qiao, Mesoporous hybrid material composed of Mn3O4 nanoparticles on nitrogen-doped graphene for highly efficient oxygen reduction reaction, Chem. Commun. 49 (2013) 7705–7707.

[16] R. Li, F. Zhang, D. Wang, J. Yang, M. Li, J. Zhu, X. Zhou, H. Han, C. Li, Spatial separation of photogenerated electrons and holes among {010} and {110} crystal facets of $BiVO_4$, Nat Commun 4 (2013) 1432.

[17] S. Mostafa, F. Behafarid, J.R. Croy, L.K. Ono, L. Li, J.C. Yang, A.I. Frenkel, B.R. Cuenya, Shape-dependent catalytic properties of Pt nanoparticles, J. Am. Chem. Soc. 132 (2010) 15714–15719.

[18] Y. Li, W. Shen, Morphology-dependent nanocatalysts: Rod-shaped oxides, Chem. Soc. Rev. 43 (2014) 1543–1574.

[19] X. Xie, Y. Li, Z.-Q. Liu, M. Haruta, W. Shen, Low-temperature oxidation of CO catalysed by Co_3O_4 nanorods, Nature 458 (2009) 746–749.

[20] J. Xiao, Q. Kuang, S. Yang, F. Xiao, S. Wang, L. Guo, Surface Structure Dependent Electrocatalytic Activity of Co_3O_4 Anchored on Graphene Sheets toward Oxygen Reduction Reaction, Sci. Rep. 3 (2013).

[21] M.P. Yeager, W. Du, Q. Wang, N.A. Deskins, M. Sullivan, B. Bishop, D. Su, W. Xu, S. D. Senanayake, R. Si, Pseudocapacitive Hausmannite Nanoparticles with (101) Facets: Synthesis, Characterization, and Charge-Transfer Mechanism, ChemSusChem 6 (2013) 1983–1992.

[22] P. Zhang, Y. Zhan, B. Cai, C. Hao, J. Wang, C. Liu, Z. Meng, Z. Yin, Q. Chen, Shape-controlled synthesis of Mn_3O_4 nanocrystals and their catalysis of the degradation of methylene blue, Nano Res. 3 (2010) 235–243.

[23] G. Kresse, J. Furthmüller, Efficient iterative schemes for \textit{ab initio} total-energy calculations using a plane-wave basis set, Phys. Rev. B 54 (1996) 11169–11186.

[24] P.E. Blöchl, Projector augmented-wave method, Phys. Rev. B 50 (1994) 17953–17979.

[25] S. Lei, K. Tang, Z. Fang, H. Zheng, Ultrasonic-Assisted Synthesis of Colloidal Mn_3O_4 Nanoparticles at Normal Temperature and Pressure, Cryst. Growth Des. 6 (2006) 1757–1760.

[26] T. Yu, J. Moon, J. Park, Y.I. Park, H.B. Na, B.H. Kim, I.C. Song, W.K. Moon, T. Hyeon, Various-shaped uniform Mn_3O_4 nanocrystals synthesized at low temperature in air atmosphere, Chem. Mater. 21 (2009) 2272–2279.

[27] H. Huang, Q. Yu, X. Peng, Z. Ye, Single-unit-cell thick Mn_3O_4 nanosheets, Chem. Commun. 47 (2011) 12831–12833.

[28] Z.H. Wang, D.Y. Geng, Y.J. Zhang, Z.D. Zhang, Morphology, structure and magnetic properties of single-crystal Mn_3O_4 nanorods, J. Cryst.Growth 310 (2008) 4148–4151.

[29] J. Duan, S. Chen, S. Dai, S.Z. Qiao, Shape Control of Mn_3O_4 Nanoparticles on Nitrogen-Doped Graphene for Enhanced Oxygen Reduction Activity, Adv. Funct. Mater. 24 (2014) 2072–2078.

[30] M. Kang, E.D. Park, J.M. Kim, J.E. Yie, Manganese oxide catalysts for NOx reduction with NH_3 at low temperatures, Appl. Catal. A: General 327 (2007) 261–269.

[31] F.H.B. Lima, M.L. Calegaro, E.A. Ticianelli, Electrocatalytic activity of manganese oxides prepared by thermal decomposition for oxygen reduction, Electrochimi. Acta 52 (2007) 3732–3738.

[32] S. Jung, C.C.L. McCrory, I.M. Ferrer, J.C. Peters, T.F. Jaramillo, Benchmarking nanoparticulate metal oxide electrocatalysts for the alkaline water oxidation reaction, J. Mater. Chem. A 4 (2016) 3068–3076.

[33] Y.L. Cao, H.X. Yang, X.P. Ai, L.F. Xiao, The mechanism of oxygen reduction on MnO_2-catalyzed air cathode in alkaline solution, J. Electroanal. Chem. 557 (2003) 127–134.